



## Zinc peroxide nanoparticles: Surface, chemical and optical properties and the effect of thermal treatment on the detoxification of mustard gas



Dimitrios A. Giannakoudakis<sup>a,b</sup>, Marc Florent<sup>a</sup>, Rajiv Wallace<sup>a</sup>, Jeff Secor<sup>c</sup>, Christopher Karwacki<sup>d</sup>, Teresa J. Bandosz<sup>a,b,\*</sup>

<sup>a</sup> Department of Chemistry, The City College of New York, New York, NY 10031, USA

<sup>b</sup> Ph.D. Program in Chemistry, The Graduate Center of the City University of New York, New York, NY 10016, USA

<sup>c</sup> Department of Physics, The City College of New York, New York, NY 10031, USA

<sup>d</sup> ECBC/CBR Filtration Branch ATTN: RDCB-DRP-F, 5183 Blackhawk Road, Bldg. 3549 APG, MD 21010, USA

### ARTICLE INFO

**Keywords:**

Zinc peroxide nanoparticles  
CEES  
Chemical warfare agents  
Detoxification  
Mustard gas

### ABSTRACT

Highly porous zinc peroxide nanoparticles were synthesized at ambient conditions following a one-pot wet precipitation method. Subsamples were calcined at various temperatures up to 400 °C. The structural, morphological, optical and chemical features were evaluated by X-Ray diffraction, N<sub>2</sub> adsorption, scanning electron microscopy, diffuse reflectance UV-vis spectroscopy, Raman spectroscopy, and thermal analysis. The degree of ZnO<sub>2</sub> decomposition to ZnO was monitored by XRD or Raman spectroscopy. The content of peroxide and the ability to form hydroxyl and super oxide radicals were also evaluated. The affinity of the synthesized samples to reactively adsorb chemical warfare agent surrogate of mustard gas, 2-chloroethyl ethyl sulfide (CEES) or ethyl ethyl sulfide (EES) was evaluated. Zinc peroxide nanoparticles were found as the best performing material, due to a high porosity and favorable surface chemistry. Moreover, they showed the ability to selectively oxidize EES to ethyl ethyl sulfoxide. In the case of CEES adsorption and subsequent reaction, the major surface reaction product was hydroxyethyl ethylsulfide (HEES). This suggests that the formation of a transient intermediate sulfonium cation is the predominant detoxification pathway. Weakly adsorbed and/or structural water enhanced the vapor retention and the decomposition performance. The ultimate task was to evaluate the detoxification performance against the real mustard gas. Zinc peroxide nanoparticles showed a marked detoxification activity with a conversion rate of 67.5%.

### 1. Introduction

From the first usage of chemical warfare agents (CWAs), there has been a search for efficient methods for the destruction/elimination of these chemical hazards. Bis (2-chloroethyl) sulfide, known as mustard gas (ClCH<sub>2</sub>CH<sub>2</sub>SCH<sub>2</sub>CH<sub>2</sub>Cl, HD), is a blister agent that has been used on multiple occasions as a chemical weapon, on civilians [1]. One of the methods to eliminate/decrease CWAs is adsorption and subsequent reaction. It can also be considered as a detoxification method. Heterogeneous catalysis in ambient conditions is an attractive method of the detoxification/mineralization of various categories of CWAs that can improve the safety of warfighters.

2-Chloroethyl ethyl sulfide (CEES), since it contains the same reactive group ( $-\text{SCH}_2\text{CH}_2\text{Cl}$ ) and is less toxic than is sulfur mustard (HD), is currently used to simulate the reactivity of the latter. Even though there are many reports on the detoxification of this surrogate in solutions of numerous solvents on various materials [2–6], the studies

on the detoxification of the surrogate's vapors or aerosols/droplets, which is in fact a physical form of this species representing the real conditions of intended applications of detoxification media, are limited [7–11]. Ethyl ethyl sulfide (EES) is another compound, which is used in the study of HD activity. EES has a similar structure to that of CEES but the chlorine atom is replaced by hydrogen ( $-\text{SCH}_2\text{CH}_3$ ). Since it has been reported by Luo et al. that chlorine atoms play a crucial role in photocatalytic oxidation due to the formation of chlorine radicals [12], comparing EES that has no chlorine to CEES with one chlorine provides good insight into HD activity.

Metal hydroxides or oxides, metal organic frameworks (MOF) and carbon-based materials have been shown to be excellent candidates for the adsorption and subsequent reaction of CWAs [8,13–25]. The most common reported pathways of HD detoxification are hydrolysis, dehydrohalogenation, oxidation and degradation/recombination [26]. Dehydrohalogenation and hydrolysis are the most often reported reaction pathways. However, both result in the formation of hydrochloric

\* Corresponding author at: Department of Chemistry and Biochemistry, The City College of New York, New York, NY 10031, USA.  
E-mail address: [tbandosz@cuny.edu](mailto:tbandosz@cuny.edu) (T.J. Bandosz).

acid and thioglycol, which are also toxic. The removal of the chlorine from HD can also poison the active centers. The use of photoreactive catalysts may lead to the formation of molecules with increased molecular weight, which are not desirable due to their toxicity. While selective partial oxidation leads to the sulfoxide derivatives that are considered as nontoxic, the sulfone derivatives from the full oxidation have vesicant properties. For this reason, the former method should be the target for developing advanced materials for the detoxification of CWAs.

It has been reported previously that pure hydrogen peroxide is a rapid oxidative decontaminant of CWA [27,28]. Thus, taking into account that current decontaminants such as hypochlorite, produce corrosive byproducts with irritant and vesicant properties, a peroxide usage as an oxidant is worth exploring [29]. Hydrogen peroxide has also proven to be a good candidate for low temperature decontamination. Thus, emulsions of peroxide have been used as CWA decontaminants at temperatures as low as  $-18^{\circ}\text{C}$  [30]. Activity at even lower temperatures has been studied showing no evidence of freezing, phase separation or precipitation [28]. Stable materials, which can form active peroxide during interactions with organic pollutants are very attractive media for CWA decontamination, especially due to their capability to oxidize these species to non-toxic products. Dionysiou et al. showed that the addition of hydrogen peroxide to titania resulted in an increase in the photocatalytic degradation rates of 4-chlorobenzoic acid in water under near-UV radiation [31,32].

The above-mentioned strong oxidizing agents were found to form sulfones. Consequently, the selective oxidation of sulfides to sulfoxides is crucial. Farha et al. have recently addressed NU-1000 MOF as a heterogeneous photocatalyst, which selectively converted CEES to sulfoxide [33]. They proposed the involvement of a singlet oxygen formed by MOF under the irradiation with ultraviolet light-emitting diode (LED), however, all the tests were held in anhydrous methanol. Another recent study showed the selective zinc-catalyzed oxidation of EES to sulfoxide in dioxane as a solvent, at room temperature, and using hydrogen peroxide as an oxidant [34].

Zinc hydroxide/oxide has been demonstrated as a good adsorbent/degradation medium of sulfur containing molecules [35–39]. Although zinc peroxide has a wide variety of applications, to the best of our knowledge, there has been no study on the CWAs detoxification on this material.  $\text{ZnO}_2$  is used in explosives, due to its oxidative properties [40], in rubber production for wear resistance [41–44], and in medicine for oral surgeries [45] and in tumor treatments [46]. Among the reported synthesis methods, the additions of hydrogen peroxide to precursors such as  $\text{ZnO}$  [47],  $\text{Zn}(\text{OH})_2$  [48],  $\text{ZnEt}_2$  [49–51],  $\text{Zn}(\text{NO}_3)_2$  [52] or  $\text{ZnCl}_2$  [53] at ambient conditions have been most often used.

The objective of this study is twofold: 1) to synthesize  $\text{ZnO}_2$  nanoparticles with high purity and increased porosity by a one-pot wet precipitation, and 2) to analyze in details their chemical, structural, morphological and optical properties and their effects on the CWAs decontamination. The thermal stability of the obtained material has been also evaluated. Various calcination temperatures are applied and the effects of the thermal treatment on the surface features and activities are evaluated. In order to derive the mechanisms of the CWAs decontamination, the ability of all synthesized samples to form hydroxyl radicals, peroxide anions and superoxide radicals under light or in the dark was investigated. Based on the analysis of the reaction products in the headspace and the extracts, the mechanisms of interactions and the formation of the surface reaction products upon contacts with CEES and EES were proposed. The ability of our materials to adsorb/react with HD was also evaluated.

## 2. Experimental

### 2.1. Materials

For the scaled up synthesis of zinc peroxide, 400 mL of  $\text{NaOH}$  (6 M)

was added to 2 L  $\text{ZnCl}_2$  solution (0.1 M) under vigorous stirring until complete dissolution. The pH was around 13. Then, 250 mL of  $\text{H}_2\text{O}_2$  30% were rapidly added. The formed precipitate was left to settle down and then washed three times with water and one time with ethanol. Finally, it was dried under vacuum at a room temperature. This sample is referred to as  $\text{ZnO}_2$ . The final mass of the synthesized material was 12.543 g (yield 64%). Around one gram subsamples of  $\text{ZnO}_2$  were further heated for 1 h in air at 130, 200, 300 and  $400^{\circ}\text{C}$  and the obtained samples are referred to as Zn130, Zn200, Zn300 and Zn400, respectively. The yields of the calcinations were 94.2, 87.2, 77.5 and 77.4%, respectively.

### 2.2. Materials characterization

#### 2.2.1. Surface area and porosity

ASAP 2020 (Micromeritics) was used to measure nitrogen adsorption isotherms at  $-196^{\circ}\text{C}$ . From them, BET surface areas were calculated. The total pore volume,  $V_{\text{Total}}$ , was obtained from the amount adsorbed at a relative pressure of 0.99 and the micropore volume,  $V_{\text{mic}}$ , was calculated from the Dubinin-Astakhov equation. The mesopore volume was calculated by the difference between the  $V_T$  and  $V_{\text{mic}}$  and the Barret-Joyner-Halenda (BJH) was used to calculate pore size distributions, PSDs. The impact of the outgas temperature on materials porosity was examined by outgassing the  $\text{ZnO}_2$  sample at  $60^{\circ}\text{C}$ , 90 or  $120^{\circ}\text{C}$  for 12 h.

#### 2.2.2. X-Ray diffraction

The X-Ray powder diffraction patterns were collected from 10 to  $70^{\circ}$  2θ at absolute scan on a Philips X'Pert X-Ray diffractometer with  $\text{CuK}\alpha$  radiation at 40 mA and 40 kV.

#### 2.2.3. Scanning electron microscopy

The Scanning Electron Microscopy (SEM) images were obtained with a FEI Helios NanoLab 660 instrument, equipped with a backscatter electrons detector and with 5 keV acceleration voltage.

#### 2.2.4. Raman spectroscopy

Raman spectra were obtained under excitation with the 488 nm laser from an argon-ion laser and dispersed by a 1200 line/mm grating using a 75 cm spectrometer with a liquid  $\text{N}_2$  cooled CCD.

#### 2.2.5. Thermal analysis (TA)

Thermogravimetric (TG), differential thermal (DTA) and derivative thermogravimetric (DTG) analyses were obtained on SDT Q600 (TA instruments) thermal analyzer under air or helium. The samples were heated at a rate of  $10^{\circ}\text{C}/\text{min}$  from room temperature up to  $1000^{\circ}\text{C}$ . A flow of 100 mL/min of He (ultra-dry) or air was held during the analyses.

#### 2.2.6. DRUV-Vis-NIR

Diffuse reflectance Ultraviolet-Visible-Near Infra-Red spectra were obtained between 300 and 800 nm using a Cary Varian spectrophotometer equipped with an integrating sphere [54].

#### 2.2.7. Surface pH

100 mg of sample was mixed with 50 mL of deionized water. The suspension was continuously stirred for 24 h, and then the pH was measured.

### 2.3. Determination of reactive oxygen species (ROSS)

#### 2.3.1. Hydroxyl radicals ( $\cdot\text{OH}$ )

The formation of hydroxyl radicals was investigated based on the fluorescence of hydroxyl terephthalate (HTA) solution. 10 mg of material were stirred in 100 mL of a 2 mM terephthalate (TA) solution. 3 mL aliquots were regularly withdrawn at specific time intervals,

filtered and their fluorescence were measured ( $\lambda_{\text{excitation}} = 312 \text{ nm}$ ). TA is non-fluorescent but it is easily hydroxylated by hydroxyl radical to form HTA, which is fluorescent. Therefore, the fluorescence intensity detected is a direct measure of the formation and the concentration of the hydroxyl radicals. The experiments were performed at ambient light irradiation and in dark.

### 2.3.2. Peroxide content

The peroxide content was quantitatively evaluated using the permanganometry redox titrations technique, where permanganate oxidizes hydrogen peroxide. The samples (100 mg) were dissolved in an acidic aqueous solution ( $\text{H}_2\text{SO}_4$ , 25 mL, 0.3 M). The weight percentage of  $\text{H}_2\text{O}_2$  in each sample was calculated based on the volume of  $\text{KMnO}_4$  (0.02 M) consumed until the titration end point.

### 2.4. CEES or EES vapor or droplets adsorption

#### 2.4.1. Vials-in-Vial closed vapor adsorption system

The adsorption of CEES or EES vapors was studied in batch experiments. A glass vial containing 20 mg of the sample was introduced into a 20 mL reaction vessel closed with a septum. After hermetically sealing the vessel, CEES (20  $\mu\text{L}$ ) was injected through a septum into another 1 mL container placed in the reaction vessel. The containers were kept under visible light at room temperature for various intervals of time. The latter was done to ensure the equilibrium of any surface reaction, to allow the complete evaporation of the vapors in the container, and to determine the maximum adsorption performance against vapors. After the equilibrium was reached, the containers were opened and the adsorbent samples were equilibrated in air for 1 h at atmospheric pressure, in the absence of moisture. Finally, the containers with the adsorbents were weighed, and the mass gain as a result of the adsorption process recorded and expressed as weight uptake (WU, mg/g).

#### 2.4.2. Droplet/conversion test

30 mg of the sample was introduced to a 20 mL vessel. Then, 3 mg of EES, CEES or mustard gas (HD) were injected directly to the surface of the material as a droplet. The vessel was tightly closed and shaken for 1 min. After 24 h, 1 mL of acetonitrile was introduced into the reaction vessel with a syringe through the septum. The vial was shaken (1 min), and afterwards the extractions were filtrated and were analyzed by GC-MS.

## 3. Results and discussion

### 3.1. Chemical, structural and morphological characterizations of $\text{ZnO}_2$ nanoparticles

X-Ray diffraction was used to identify the crystallographic phases. The XRD pattern of the as-synthesized powder (Fig. 1A) revealed a single-phase of cubic zinc peroxide with space group  $\text{Pa}-3$ . The positions of all diffraction peaks match those of the standard card JCPDS-13-0311 [52,55]. The four dominant diffraction peaks are at 31.91, 37.26, 53.15 and 63.31  $2\theta$  and they can be respectively indexed as (111), (200), (220) and (311) [50,56]. The intense but broad diffraction peaks suggest the existence of nano-crystallites of zinc peroxide [57,58]. Thus the basic environment lead to the transformation of the excess of  $\text{H}_2\text{O}_2$  to peroxide anions ( $\text{O}_2^{2-}$ ), which then react with the zinc cations and results in the precipitation of  $\text{ZnO}_2$ .

The evaluation of porosity by  $\text{N}_2$  adsorption showed that  $\text{ZnO}_2$  has a relatively large surface area ( $111 \text{ m}^2/\text{g}$ ) and high total pore volume ( $0.287 \text{ cm}^3/\text{g}$ ). These results are in the range of those reported in the literature for zinc peroxide [58]. The gradual curvature at low  $p/p_0$  (Type II(b) isotherm) [59] is related to a limited volume of micropores (6.6% of the total pore volume). The pore size distribution (Fig. 1B, inset), obtained using BJH method, shows the heterogeneity of pore

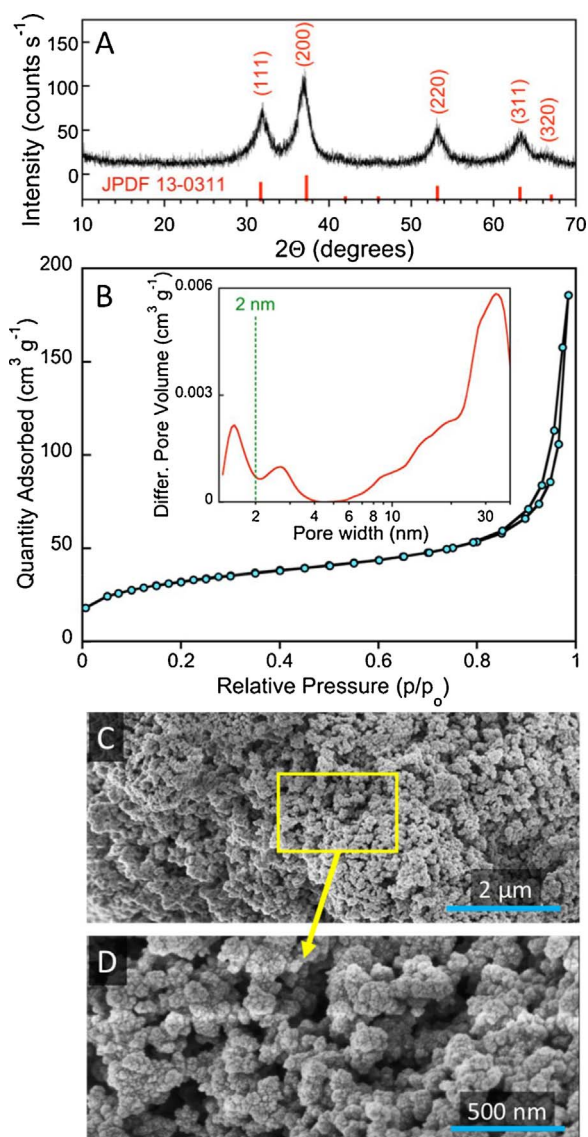


**Fig. 1.** XRD pattern of  $\text{ZnO}_2$  nanoparticles. The red tick-marks indicate the positions of the diffraction peaks corresponding to the standard card JCPDS-13-0311 of cubic-structured  $\text{ZnO}_2$ ; (A) the nitrogen adsorption isotherm; (B) and the pore size distribution (inset), (C) SEM; (D) HR-SEM images of  $\text{ZnO}_2$ . (For interpretation of the references to color in this figure legend, the reader is referred to the web version of this article.)

sizes, with very small volumes of micropores (< 2 nm) and of small mesopores (< 4 nm), and a broad size distribution of large mesopores, with a predominant pore of about 30 nm. The average pore width derived from PSD is 10.6 nm. A small Type H3 hysteresis loop indicates that the pores do not have a complex structure [59]. The porosity of our samples is similar or even higher than those of various metal (hydr) oxides, such as  $\text{Zr}(\text{OH})_4$ ,  $\text{Fe}(\text{OH})_3$  and  $\text{Zn}(\text{OH})_2$ , which showed a good adsorption performance against CWAs surrogates [60–62].

The SEM images of  $\text{ZnO}_2$  (Fig. 1C, D) show agglomerates of small nanospheres with sizes of about 100–250 nm. Moreover, the macropores of various diameters between the aggregates are seen. These macropores can have a crucial effect on the adsorption/catalytic process, since they can promote the diffusion of the molecules inside the micro- and meso- pores.

The thermal gravimetric (TG), differential thermal gravimetric (DTG) and differential thermal analysis (DTA) curves are presented in Fig. S1. The DTG curves reveal two predominant peaks. The endothermic one, in the range of 30–130 °C with a maximum at 75 °C, is linked to the release of adsorbed water. It represents only 4.1% weight

loss. The exothermic one, in the range between 150 and 300 °C with a maximum at 219 °C, represents an oxygen removal during the transformation of the peroxide phase to oxide [56]. This is the predominant weight loss of 16.2% for this material. Taking into account that a theoretical weight loss for the decomposition of  $\text{ZnO}_2$  to  $\text{ZnO}$  is 16.4%, the results obtained indicate that the synthesized bulk material contains the peroxide structure. This is in agreement with the XRD results.

### 3.2. Calcination at different temperatures

To evaluate thermal stability in air and the effect of the calcination temperature on the structural and chemical properties,  $\text{ZnO}_2$  was heated at four temperatures for 1 h: 130 °C was chosen to remove the structural and weakly adsorbed water molecules; 200 °C – to achieve “intermediate” decomposition stage, where both peroxide and hexagonal oxide phases coexist; 300 and 400 °C – to completely transform  $\text{ZnO}_2$  to the oxide phase. The calcination of zinc peroxide resulted in a small increase in the surface pH with an increase in the temperature. The surface pH of the pristine sample was 9.36, and after heating at 130, 200, 300 and 400 °C it slightly increased to 9.47, 9.52, 9.76 and 9.94, respectively.

The transformation path of peroxide to oxide was monitored primarily by X-ray diffraction (Fig. 2A). Two diffraction peaks characteristic of each phase ( $\text{ZnO}_2$  and  $\text{ZnO}$ ) were selected to monitor the changes (Fig. 2B). The calcination temperature of 130 °C did not alter the peroxide crystallinity. The only difference is the limited broadening of the peaks due to a decrease in the crystal sizes. The intensities of the diffraction peaks related to the peroxide phase remained unchanged.

Interestingly, the calcination temperature of 200 °C led to the partial conversion of the peroxide into the hexagonal oxide and to the coexistence of two phases. The intensities of all peaks were low due to the

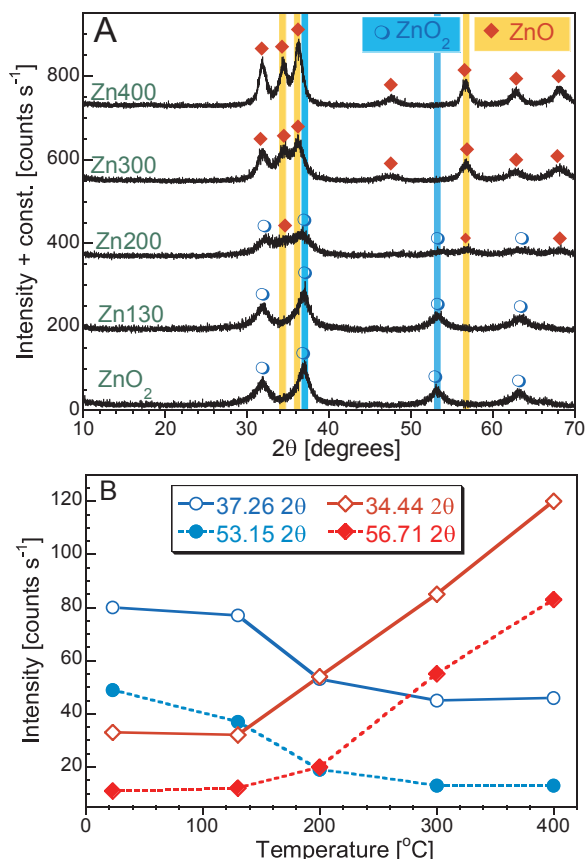


Fig. 2. A) XRD patterns for initial  $\text{ZnO}_2$  and the calcined samples and B) the evolution of the intensity of the peaks representing the peroxide (37.26 and 53.15 2θ) and oxide phase (34.44 and 56.71 2θ).

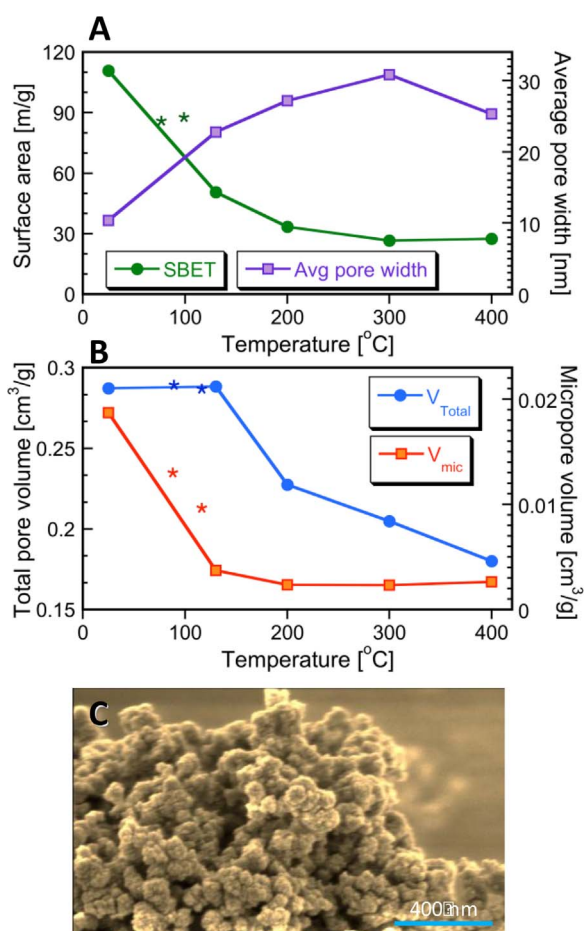


Fig. 3. Analysis of the porous structure and texture: surface area and average pore width (A), total pore volume and micropores volume (B), and SEM image of Zn400 (C). The asterisks mark the values of the parameters of the pores structure calculated after degassing at 90 and 120 °C.

pure crystallinity of both phases. At this stage, the peroxide crystals almost disappeared and the oxide crystals started to grow. Higher calcination temperatures caused further disappearance of the diffraction peaks related to the peroxide phase and the appearance of well-defined peaks of the oxide structure. The intense peaks at 34.44, 36.21, 47.69, 56.57 and 68.17 2θ seen on the diffractograms of the samples calcined above 200 °C along with the two peaks at 31.7 and 63.21 2θ, which overlap with the peroxide phase, indicate the wurtzite structure of zinc oxide (JCPDS 36-1451) [63,64]. It is worth to mention that the intensities of the characteristics peaks of the latter phase increase even more with an increase in the calcination temperature to 400 °C. The relative intensities of the three diffraction peaks between 30 and 40 2θ suggest no preferred orientation and spherical wurtzite structured nanocrystals [65].

The effect of the calcination temperature on the porous structure was also studied. The results obtained from the  $\text{N}_2$  adsorption isotherms are collected in Fig. 3. The sample calcined at 130 °C showed a markedly lower surface area ( $51 \text{ m}^2 \text{ g}^{-1}$ ) than the initial  $\text{ZnO}_2$  sample. A further increase in the calcination temperature decreased further the surface area and the samples prepared at 300 and 400 °C reach only about  $26 \text{ m}^2 \text{ g}^{-1}$ . Interestingly, although the calcination at 130 °C did not alter the total pore volume ( $V_{\text{Total}}$ ), the limited volume of the micropores of  $\text{ZnO}_2$  totally vanished. The SEM image of Zn400 (Fig. 3C) shows that the calcination, even at 400 °C, did not change the structure of the particles. The samples consist of 50–250 nm aggregates of spherical nanoparticles with voids of various sizes (in the range of macropores) between the aggregates.

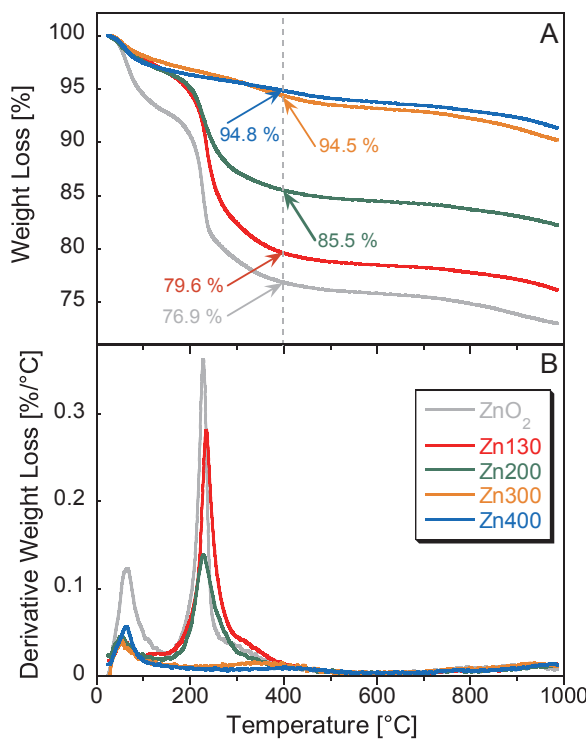


Fig. 4. TG (A) and TDG (B) curves measured in air.

In order to explore the porosity changes in the  $\text{ZnO}_2$  phase, the degassing before the nitrogen adsorption measurement was carried out also at 90 and 120 °C. The asterisks on the diagrams in Fig. 3 mark the values of the structural parameters measured in these experiments. Degassing at 90 and 120 °C decreased the surface area of about 25%. The total pore volume was not affected. We link this to the increased pore sizes upon thermal treatment. The large mesopores between aggregates were transformed to macropores and the micropores- to small mesopores. This is likely due to crystallographic phase transformations.

The differences in surface chemistry and in thermal stability of the samples were examined by thermal analysis. The TG and DTG curves are collected in Fig. 4. For all samples studied, the weight loss up to 60 °C was less than 1% and up to 130 °C – less than 3%, except for  $\text{ZnO}_2$  for which it was 4.1%. The thermal decomposition of the samples that contain the zinc peroxide phase ( $\text{ZnO}_2$ ,  $\text{Zn130}$  and  $\text{Zn200}$ ) started above 180 °C. For the sample with no peroxide phase, the total weight losses were less than 10%, even up to 1000 °C. Interestingly, the difference in the weight loss at 400 °C for  $\text{Zn200}$  and  $\text{Zn400}$  is 9.3%. This value represents almost half of the difference in the weight losses between  $\text{ZnO}_2$  and  $\text{Zn400}$ , suggesting that almost half the peroxide phase decomposed to oxide during calcination.

To gain more insight into the oxygen arrangement in the samples, Raman spectra were collected (Fig. 5A). Raman spectroscopy detect O–O vibrations, which are not visible in infrared spectroscopy. Indeed, since the unit cell of  $\text{ZnO}_2$  possesses an inversion center, its vibrational modes cannot be both Raman and infrared active based on the rule of mutual exclusion [55]. The spectrum of  $\text{ZnO}_2$  revealed a predominant strong peak centered at  $840.7\text{ cm}^{-1}$ , which is linked to the stretching mode of the O–O bond of the peroxy ion ( $\text{O}_2^{2-}$ ) [66], and three peaks with lower intensity at  $1080.8$ ,  $476.2$  and  $414.2\text{ cm}^{-1}$ . Analogous Raman active modes have been reported for inorganic bulk peroxides, such as  $\text{BaO}_2$  and  $\text{ZnO}_2$  [55].  $\text{Zn130}$  showed exactly the same pattern of the active modes as  $\text{ZnO}_2$ , further supporting the minimal removal of water molecules. The spectrum of the sample calcined at 200 °C shows the same peaks but of markedly lower intensities. Moreover, the typical vibration modes of wurtzite zinc oxide are also visible [67]. The intensities of these peaks at  $1152.9$  (medium),  $582.1$  (medium),  $437.7$

(strong) and  $333.6$  (weak)  $\text{cm}^{-1}$  increase for the samples calcined above 200 °C [68,69]. Two vibration modes at  $1080.8$  and  $414.2\text{ cm}^{-1}$  are also found in the spectra for all samples, linked to the vibration modes of Zn–O bonds [70]. Therefore, the relative intensities of the modes at  $840.7$  and  $582.1\text{ cm}^{-1}$  can be used to qualitatively characterize the ratio of the different oxygen vacancies based on Raman spectroscopy.

The optical properties of the samples tested were evaluated using the Diffuse Reflectance UV-vis-NIR absorption (Fig. 5B). The spectra of  $\text{ZnO}_2$  and  $\text{Zn130}$  displayed limited absorption of photons in the whole studied electromagnetic range. The other three samples show a marked photon absorption for wavelength lower than 430 nm. The band gaps ( $E_g$ ) were estimated based on the Kubelka-Munk model from the extrapolation of the linear fit of Tauc plots of  $[F(R\infty) h\nu]^2$  versus the photon energy (Fig. 5C) [71–73]. Only the samples prepared at 200 °C and above showed  $E_g$  values in the visible-light range, and in the range of other  $\text{ZnO}$  materials reported in the literature [8,74–76]. The decrease of  $E_g$  with an increase in the heat treatment temperature can be linked to the decreasing particle size and the elimination of the content/traces of the zinc peroxide phase. It was reported that a small particle size of  $\text{ZnO}$  decreases the band gap and increases activity [77]. Based on the results collected, only the samples containing the oxide phase are expected to be photoactive under visible light irradiation.

### 3.3. Estimation of reactive oxygen species

In order to gain more insights into the reactive oxygen species (ROS), which can be involved into the detoxification/decomposition reaction on our catalysts, the ability of the samples to generate hydroxyl radicals, superoxide radicals, and  $\text{H}_2\text{O}_2$  was evaluated at ambient light and in dark. The ability to promote the formation of hydroxyl radical ( $\text{OH}\cdot$ ) was examined analyzing the fluorescence intensity of hydroxyl terephthalate (HTA) after various time intervals (10, 30, 60 and 120 min). In the presence of hydroxyl radicals, terephthalate can be converted to HTA. Only the later has a characteristic emission at  $425\text{ nm}$  [77]. Fig. 6A shows the changes in the intensity of the emission at  $425\text{ nm}$  from the fluorescence spectra of the TA solution mixed with the zinc-based materials. These results clearly demonstrate that the fluorescence intensity increases only for the samples, which consist of  $\text{ZnO}$  and have the ability to form  $\cdot\text{OH}$ . These results are in agreement with the indirectly estimated sizes of the band gaps. It is important to mention that  $\text{Zn200}$ , which contains both phases, revealed a lower formation rate of HTA than did  $\text{Zn300}$  and  $\text{Zn400}$ . For  $\text{ZnO}_2$  no change in the intensity of the emission was found. The small fluorescence emission in the case of  $\text{Zn130}$  can be linked to the minimal transformation of the peroxide phase to oxide. The tests were carried out also in dark and the intensities of the peak at  $425\text{ nm}$  are collected in Fig. 6B.

Permanganometry/redox titration was used for the quantitative determination of the amount of  $\text{H}_2\text{O}_2$  released by each sample upon dissolution (Fig. 6D).  $\text{ZnO}_2$  and the sample after calcination at 130 °C released the same amounts of hydrogen peroxide. The amount of  $\text{H}_2\text{O}_2$  in the sample treated at 200 °C was 45% less than that in  $\text{ZnO}_2$ . No hydrogen peroxide formation was detected in the samples calcined at 300 and 400 °C.

### 3.4. Adsorption/surface reactivity with CEES and EES vapors

To evaluate the ability of our samples to adsorb vapors and to react with the mustard gas surrogates, 2-chloroethyl ethyl sulfide (CEES) and ethyl ethylsulfide (EES), the weight uptake tests were performed using the previously reported close vials-in-vial system [62]. After the exposure to vapors of CEES or EES for 24 h at ambient light, the differences in the weight uptakes (WU in mg/g) were measured. It is important to mention that these values are expected to represent either the amounts of vapors of the surrogates or of its degradation products, if any, adsorbed on the surface. The results for CEES adsorption after

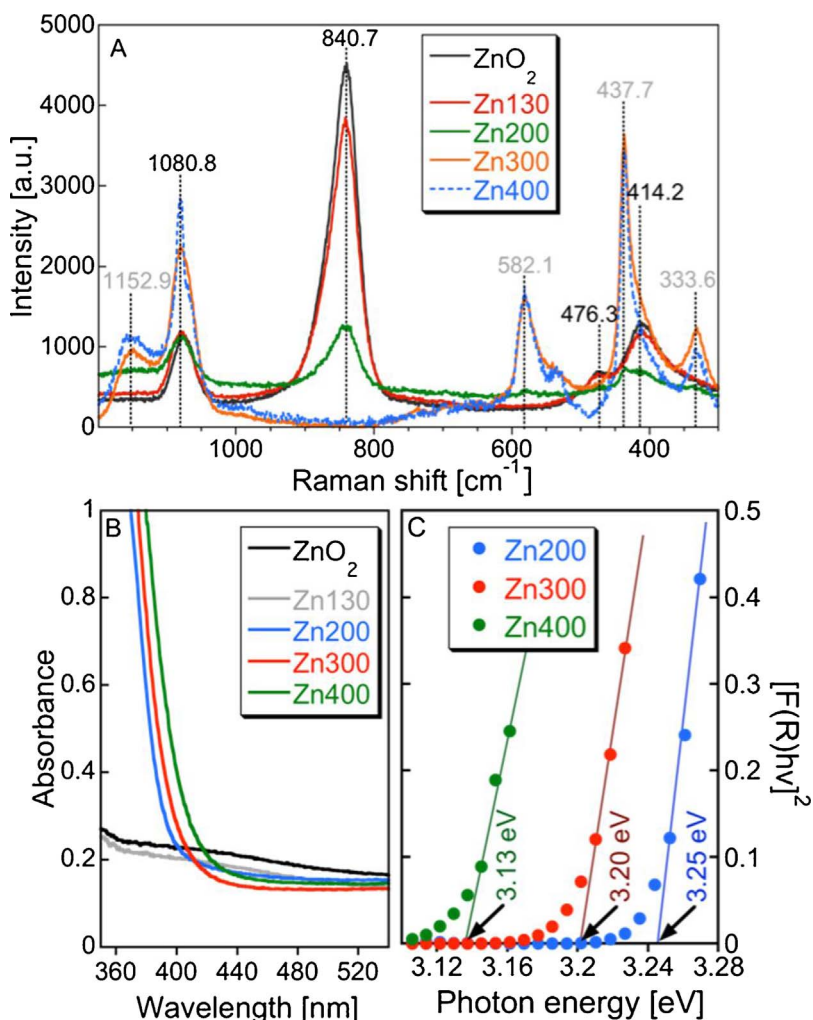


**Fig. 5.** Raman spectra (A), diffuse reflectance UV-vis-NIR absorption spectra (B) and Tauc plots (C) obtained at room temperature.

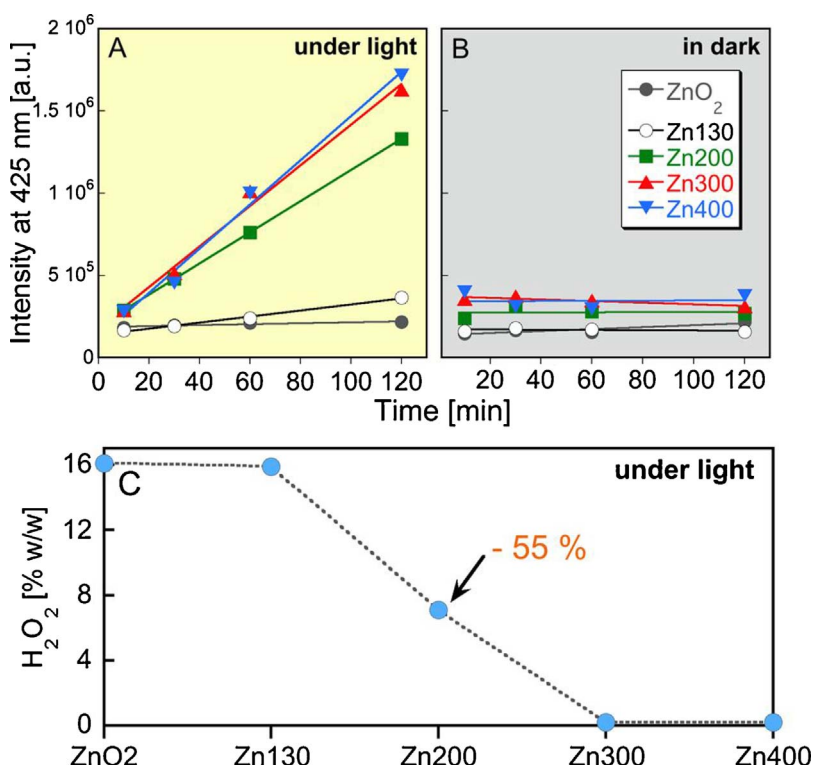


**Fig. 6.** Analysis of the changes in the intensity of the emission at 425 nm (formation kinetics of THA) with an increase in the experimental time under ambient light irradiation (A) or in dark (B), and the quantitative determination of the weight percentage of H<sub>2</sub>O<sub>2</sub> released from the samples estimated by permanganometry redox titration (C).

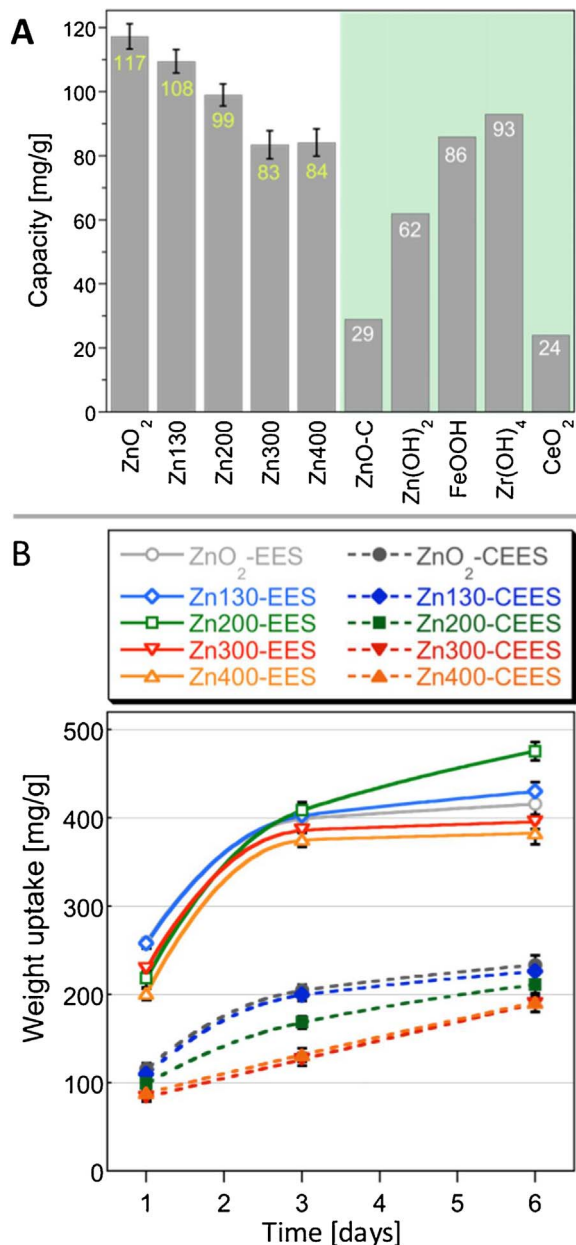


**Fig. 7.** A) weight uptakes of all the studied samples and the reported values for previously reported metal (hydr)oxide tested at the identical conditions [8,60–62,78], and B) Weight uptakes after exposure to EES and CEES vapors for 1, 3 and 6 days.

24 h of exposure are collected in Fig. 7A. For comparison, the weight uptakes reported for other metal (hydr)oxides measured at the same conditions, such as commercial ZnO nanoparticles (ZnO-C) [8], and synthesized in our lab Zn(OH)<sub>2</sub> [62], ferrihydrite (FeOOH) [61], Zr(OH)<sub>4</sub> [60], and cerium oxide (CeO<sub>2</sub>) [78] are also included. The highest capacity is found for initial ZnO<sub>2</sub>. The thermal treatment at 130 °C decreased the weight uptake by 8%. Even though this can be a result of the smaller surface area of Zn130 than that of ZnO<sub>2</sub>, the decrease in WU is much smaller than the decrease in the surface area (~50%). On Zn200, WU decreased 15% compared to that on ZnO<sub>2</sub>, while the total decomposition to zinc oxide resulted in 29% smaller weight uptakes on Zn300 and Zn400, compared to that on ZnO<sub>2</sub>. Notably, ZnO<sub>2</sub> showed the greatest performance as the CEES/decomposition product adsorbent and better than any single metal (hydr)oxide, which has been examined so far at the identical experimental conditions.

It is important to point out that no correlation between the weight

uptake and any structural feature was found (Figs. S2 and S3). The lack of a linear dependence of WU on the surface area suggests that other factors than physical adsorption must play a role in the interactions of CEES with the materials tested. As discussed above, calcination even at a low temperature results in the formation of limited quantity of ZnO on which the OH radicals are formed. The rate of the radical formation was much higher on Zn200 than that on Zn130. While Zn130 has a higher content of H<sub>2</sub>O<sub>2</sub> than has Zn200, the latter sample has a band gap of 3.25 eV, indicating the photoactivity in visible light. This photoactivity, by promoting degradation through radicals' formation, might compensate the negative effects of a small surface area on the physical adsorption of CEES.

The differences in the weight uptakes of the samples exposed to CEES were measured for up to 6 days. The recorded weight uptakes are presented in Fig. 7B. The evolution of the weight uptakes as a result of the interaction with CEES (dashed lines) showed that after 24 h of interactions, the samples consisting of only the peroxide phase (ZnO<sub>2</sub> and Zn130) had improved ability to retain vapors than those consisting of the pure oxide phase. The Zn200 sample, which contains both phases, shows WU after 24 h in the middle range of measured values. The same trend can be seen for the tests performed for 3 and 6 days, but ZnO<sub>2</sub> and Zn130 almost reached the saturation point after 3 days. On the contrary, the weight uptake on Zn130, Zn200, and Zn400 continuously increased. We link this continuous WU increase to the higher reactivity of the peroxide groups than that of the oxide groups and to the significantly higher surface areas of ZnO<sub>2</sub> and Zn130 than those of the other samples. Moreover, under photochemical excitation conditions, zinc oxide was shown previously to promote the photodecomposition of CEES to various smaller molecules, via the formation of the transient cyclic sulfonium cation [8]. Most of them are volatile and can be transferred to the headspace instead of being retained on the surface.

In order to determine which features of the samples tested play the most crucial role in the adsorption and subsequent reaction, the samples were exposed to ethyl ethylsulfide (EES, CH<sub>3</sub>CH<sub>2</sub>SCH<sub>2</sub>CH<sub>3</sub>), a molecule of the same structure as that of CEES, except the absence of the chlorine atom. The weight uptakes are collected in Fig. 7B.

After one day of interactions, ZnO<sub>2</sub> and Zn130 showed again higher WU values than other two samples. Interestingly, the differences in WU after 3 days almost vanished. It is worth to mention that the weight uptake of ZnO<sub>2</sub> and the samples calcined above 300 °C reached a maximum after 3 days of EES exposure. This trend does not exclude the possibility that the materials still interact with the vapors and further catalytically degrade them. On the other hand, the weight uptake on ZnO<sub>2</sub>, Zn130 and Zn200 kept increasing slowly even after 3 days. This can be linked to the formation of new surface reaction products, owing to the catalytic effects, which are retained on the surface. Furthermore, the highest capacities recorded on the samples consisting of both peroxide and oxide phase suggest the synergistic effect of the combination of these two phases. The slightly higher weight uptake on Zn130 than that on ZnO<sub>2</sub> can be linked to the absence of water on Zn130. These results suggest that the porosity does not play the most crucial role on the weight gain in the case of EES adsorption, as discussed above in the case of CEES.

### 3.5. Conversion on CEES and EES liquids

The most crucial outcomes from the comparison of the weight uptakes results between CEES and EES are: 1) the weight uptakes of EES were almost twice higher than those upon exposure to CEES; 2) the weight uptake kinetics were similar for all samples exposed to EES adsorption, while in the case of CEES exposure the trend in WU uptake were affected by the samples' chemistry. These two findings suggest that EES and CEES interact differently with the surface of our samples. It is also plausible that the degradation of CEES molecules is more advanced than that of EES. In order to determine if this scenario can explain the differences in WU between EES and CEES, the activity of the

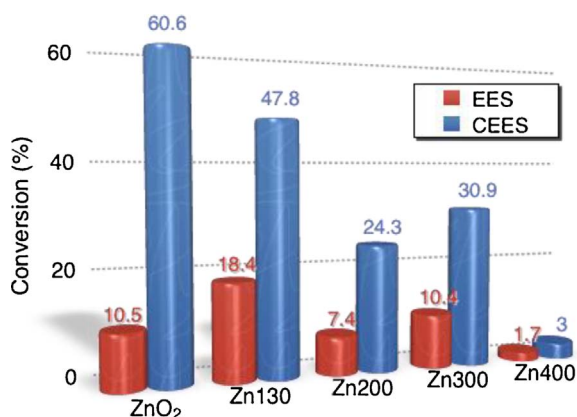


Fig. 8. Conversions ratios of EES and CEES measured by droplet tests.

samples was tested by the injection of a droplet of each surrogate directly on the powder in the closed systems. The obtained conversion results are collected in Fig. 8. The results indicate that the conversion ratio of CEES is dramatically higher than that of EES for all samples. The highest conversion ratio of CEES was obtained on ZnO<sub>2</sub>. The removal of water molecules and the decrease in the porosity after calcination at 130 °C led to a decrease in the conversion ratio by 21% for Zn130, compared to that on ZnO<sub>2</sub>. Calcination at higher temperatures and transformation of peroxide further decreased the catalytic conversion ability. In the case of EES, Zn130 showed 75% higher conversion ratio compared to that on ZnO<sub>2</sub>. This fact suggests that for the conversion of EES, the lack of water molecules is a positive factor. Another outcome of the conversion tests is that Zn400 showed ultimately lower conversion ratio compared to that on Zn300. The only difference between them is that the former sample has well crystallized particles of zinc oxide as can be seen at the XRD patterns (Fig. 2), while Zn300 is more amorphous.

### 3.6. Determination of the surface reactions products after exposure to CEES and EES

The acetonitrile extracts of the samples exposed to CEES and EES droplets were analyzed by GC-MS in order to determine the compounds retained on the surface and the involved detoxification mechanisms. All the detected compounds, along with their chemical formulas, abbreviations and the characteristics mass-to-charge ratios used for the identification, are collected in Table 1. It is worthy to point out that all the formed surface reaction products are non-toxic.

The chromatograms of the extracts of the samples exposed to CEES are presented in Fig. 9A–C. The detected compounds, besides unreacted CEES, are hydroxyl ethyl ethylsulfide (HEES), ethyl vinyl sulfide (EVS) and 1,2-bis(ethylthio) ethane (BETE), which are the hydrolysis, dehydrohalogenation and degradation/dimerization products, respectively. The comparison of the peaks' areas (Fig. 9d) indicates ZnO<sub>2</sub> as the

sample on which the least CEES and the most HEES is detected. This is in agreement with the highest CEES conversion ratio on this sample. Smaller amount of HEES and higher of CEES detected on Zn130, compared to those on ZnO<sub>2</sub> indicate the lower detoxification ability of this sample due to the smaller porosity and the absence of structural or weakly adsorbed water molecules. The transformation of the peroxide to oxide phase leads to a further diminishing of the detoxification ability, since the area related to CEES increases and the area of HEES decreases. In the case of Zn300, the area of the peaks representing EVS and BETE are noticeably higher than those for other samples. This is linked to the ability of this sample to form radicals while exposed to ambient light. Further calcination to 400 °C result in the almost total loss of the detoxification ability. The detection of ethyl vinyl sulfoxide is indicative of the oxidation ability only of the ZnO<sub>2</sub> sample. Even though CEES underwent reactions to HEES and EVS predominantly through hydrolysis, the oxidation of the latter compound to oxide ethyl vinyl sulfoxide (EVSO) is also detected. That detection of EVSO only in the case of ZnO<sub>2</sub> also suggest that the presence of structural or weakly adsorbed water molecules promote the oxidation process.

The chromatograms of the extracts from the samples exposed to EES (Fig. 9E–G) revealed the formation of the oxidation product, diethyl sulfoxide (EESO) on the zinc peroxide samples, while on the calcined sample at temperature higher than 200 °C only traces of EESO were detected. ZnO<sub>2</sub> shows a much higher oxidation ability than the sample treated at 130 °C. We link this to the presence of water, which seems to play a key role in the oxidation process. In order to exclude the possibility that the detected sulfoxide is formed only during the extraction process, the headspace of the closed adsorption system was also analyzed. EESO was detected there. On the other hand, the zinc oxide phase in samples Zn200, Zn300 and Zn400 favors the formation of diethyl disulfide (DEDS), and does not favor the oxidation process. The formation of disulfide indicates the involvement of radical's reactions as a result of the photoreactivity of these samples at visible light, which is consistent with the analysis of the UV-vis spectra and the estimated band gaps. DEDS was reported previously as a surface reaction product of radical reactions on photoactive materials such as TiO<sub>2</sub> and ZnO [8,79].

### 3.7. Detoxification mechanisms of CWAs' surrogates

The differences in surface reaction products, between the samples consisting of peroxide and those of the oxide phase, suggest differences in the nature of the involved reactions. Based on the results collected, the reactions which take place during ZnO<sub>2</sub> or Zn130 exposure to EES or CEES are presented in Scheme 1. The predominant pathways in the case of EES involve first the formation of the ethyl ethylsulfide cation (EES<sup>+</sup>) upon the interaction of the EES molecule with a Lewis acid Zn active center. The detection of a solitary product in a high concentration at the extracts of the peroxide consisting samples suggests the involvement of the O–O<sup>–</sup> group in the oxidation process, as can be seen in Pathway A1. Since the ability of these two samples to produce

Table 1

Details on the detected compounds at the extracts after exposure to CEES or EES droplet.

Name	Chemical formula	Abbrev.	Retention Time (min)	Characteristic mass-to-charge ratio ( <i>m/z</i> )
CEES droplet				
2-chloroethyl ethyl sulfide	CH <sub>3</sub> CH <sub>2</sub> SCH <sub>2</sub> CH <sub>2</sub> Cl	CEES	4.97	124, 109, 90, 75, 61, 47
hydroxyl ethyl ethyl sulfide	CH <sub>3</sub> CH <sub>2</sub> SCH <sub>2</sub> CH <sub>2</sub> OH	HEES	4.91	106, 90, 75, 61, 47
ethyl vinyl sulfide	CH <sub>3</sub> CH <sub>2</sub> SCH=CH <sub>2</sub>	EVS	1.83	88, 73, 59, 45
ethyl vinyl sulfoxide	CH <sub>3</sub> CH <sub>2</sub> SOCH=CH <sub>2</sub>	EVSO	5.21	104, 88, 76, 59, 47
1,2-bis(ethylthio) ethane	CH <sub>3</sub> CH <sub>2</sub> SCH <sub>2</sub> CH <sub>2</sub> SCH <sub>2</sub> CH <sub>3</sub>	BETE	11.85	150, 122, 90, 75, 61, 47
EES droplet				
ethyl ethyl sulfide	CH <sub>3</sub> CH <sub>2</sub> SCH <sub>2</sub> CH <sub>3</sub>	EES	1.88	90, 75, 61, 47
ethyl ethyl sulfoxide	CH <sub>3</sub> CH <sub>2</sub> SOCH <sub>2</sub> CH <sub>3</sub>	EESO	7.09	106, 93, 90, 76
Diethyl disulfide	CH <sub>3</sub> CH <sub>2</sub> SSCH <sub>2</sub> CH <sub>3</sub>	DEDS	4.86	122, 94, 66, 60, 47, 45

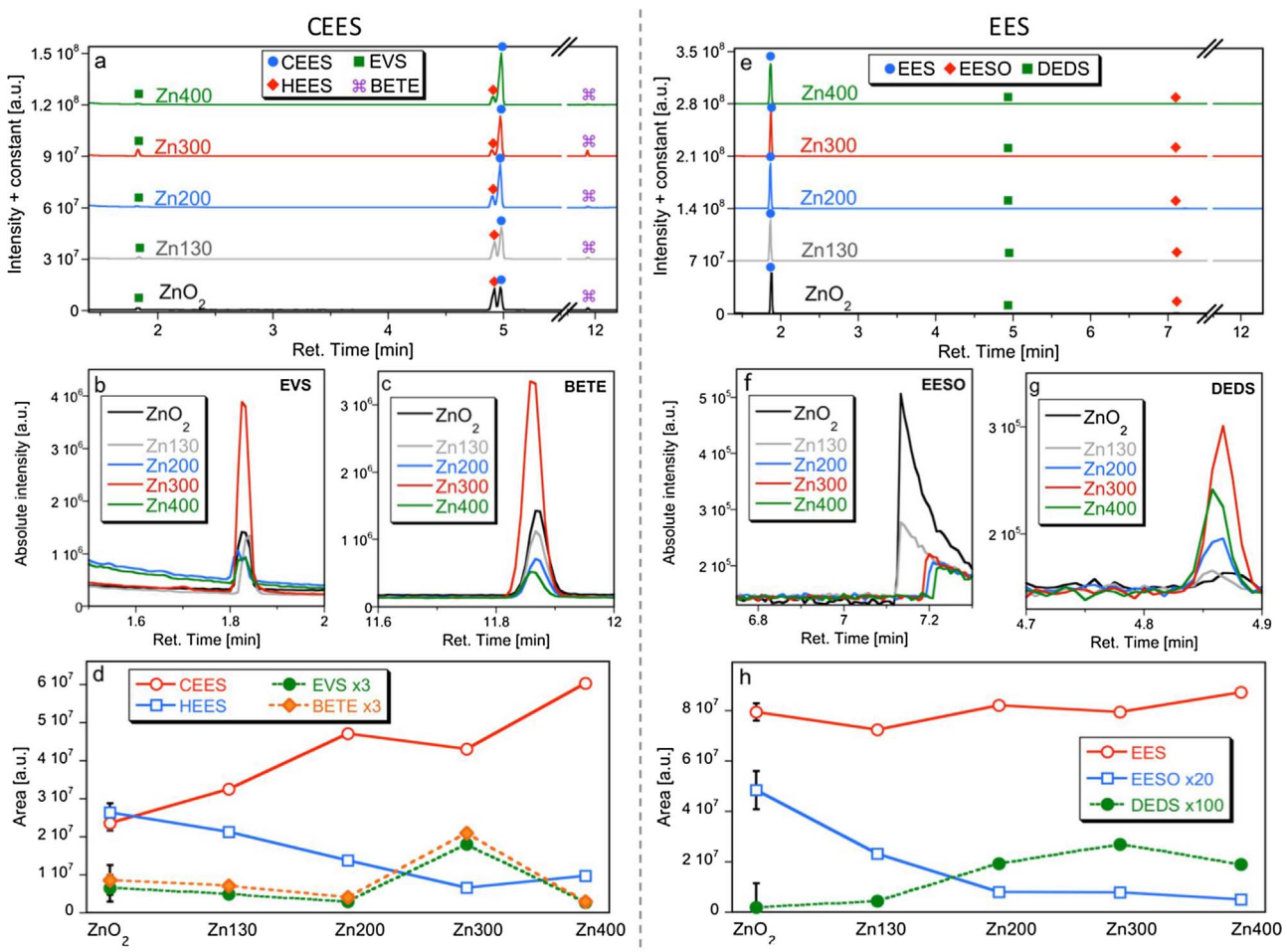


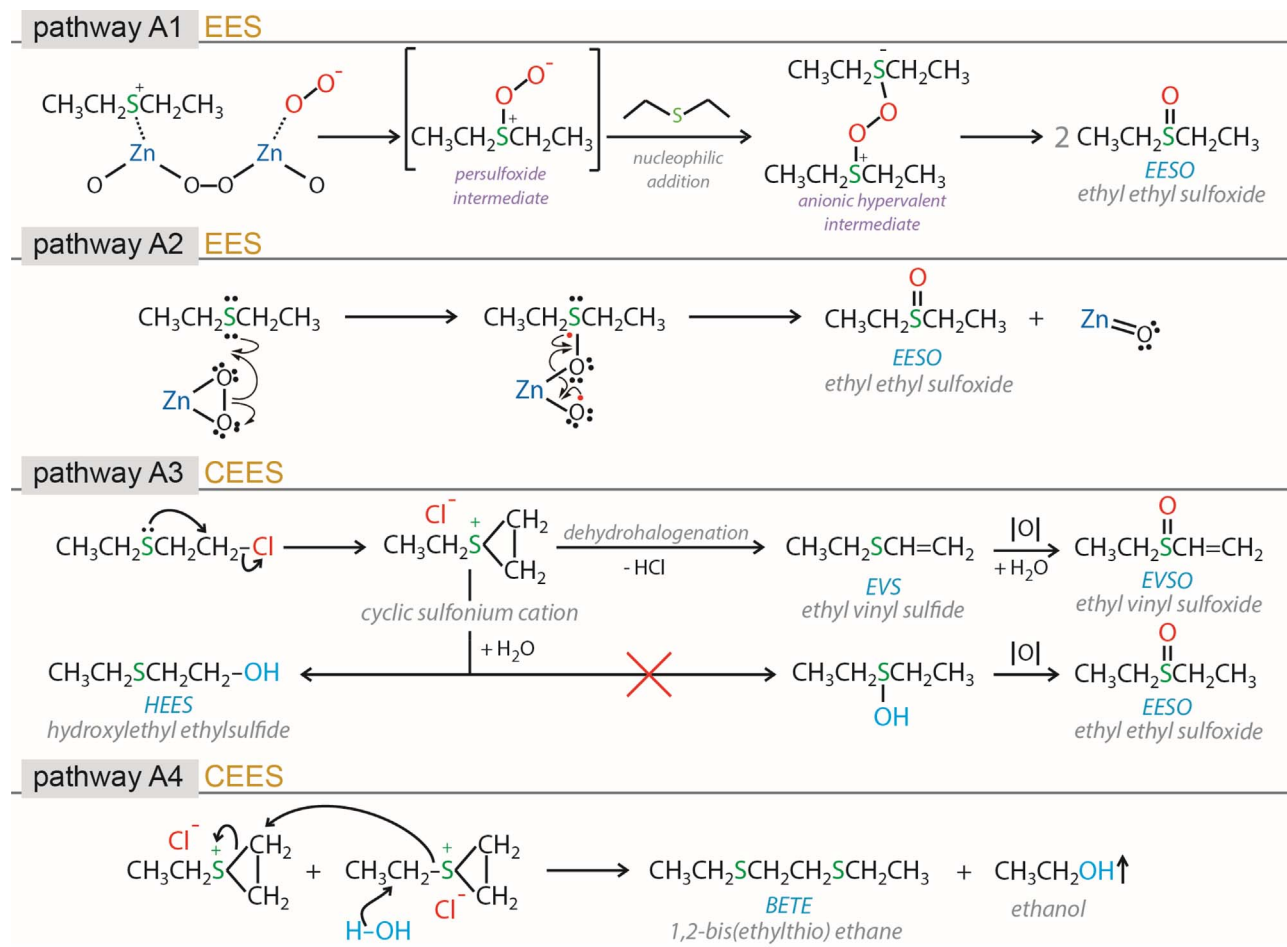
**Fig. 9.** Chromatograms of the extracts from the samples exposed to CEES (a–c) or EES (e–g) droplets and the areas of the chromatographic peaks of the detected compounds in the extracts (d, h).

peroxide is not equal (Fig. 6F), the existence of water molecules and/or the extended surface area of ZnO<sub>2</sub> might affect positively this pathway. Farha et al. showed that CEES and the real mustard gas can be selectively oxidized to nontoxic sulfoxide, without the formation of the toxic sulfones, via the formation of singlet oxygen generated from MOF (NU-1000) using ultraviolet light-emitting diode (LED) [33]. Analogously, the formation of EESO can be described by the direct interaction of the peroxide phase with EES, through electron rearrangements (Pathway A2). The absence of sulfones in the extracts supports our hypothesis that zinc peroxide almost selectively oxidizes EES to non-toxic EESO.

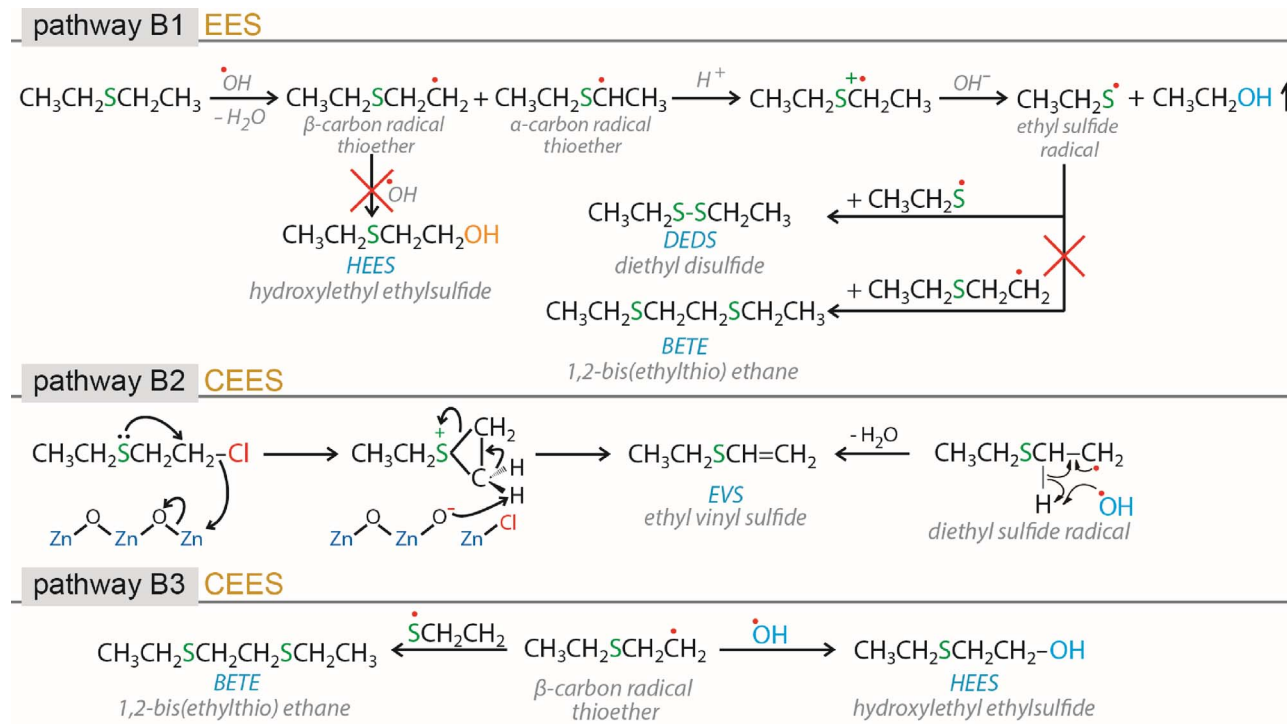
The interactions of ZnO<sub>2</sub> and Zn130 with vapors of CEES lead to formation of different products than those in the case of EES vapors: HEES, EVS, and BETE. The mechanisms their formation involve, as a first step, the physical adsorption of CEES on the surface via polar forces [80,81]. This adsorption triggers the transformation of CEES to a transient cyclic sulfonium cation by an intermolecular cyclization process, where sulfur atom, as a nucleophile, attacks the electrophilic carbon to which the chloride is bonded (Pathway A3). This cyclic cation can possibly follow three different decomposition pathways. The first one is the dehydrohalogenation, where a labile hydrogen from the cyclic cation transfers to a negatively charged lattice oxygen of the zinc peroxide phase, which acts as a Lewis base, via a bimolecular elimination (E2) reaction, in order to form EVS. A similar degradation pathway was reported for the adsorption of CEES or HD on aluminum oxide, zinc hydroxide, zirconium oxide/hydroxide and iron oxyhydroxide. The second one involves the reaction of the intermediate cyclic sulfonium cation with water at two different sites, and results in HEES

or EESO. Since only HEES was detected in the extracts, it is plausible to conclude that the hydroxyl group favors to attack a carbon instead of sulfur (Pathway A3). Finally, the transient cyclic cation can react with another cyclic cation in order to form BETE (Pathway A4). Comparison of the areas of the chromatographic peaks of HEES, EVS and BETE suggests that the cyclic cation predominantly reacts with water to form the hydrolysis product, HEES. Additionally, the higher peak area of HEES in the case of ZnO<sub>2</sub> than that in the case of Zn130 supports that water molecules promote the direct hydrolysis of CEES to HEES. The absence of EESO after exposure of ZnO<sub>2</sub> or Zn130 to CEES indicates that hydrolysis is favorable and/or faster than oxidation. This can be linked to the formation of the intermediate transient cyclic cation after the removal of the chlorine atom, which undergoes hydrolysis rapidly. It is important to mention that EES is only oxidized to sulfoxide. Additional oxidation of sulfoxide to sulfone is not desirable, since ethyl ethylsulfone has similar toxicity with mustard gas.

The formation of the oxide phase imparts to the samples photoactivity by the generation of e<sup>-</sup>/h<sup>+</sup> pairs upon the light absorption. Zinc oxide has been reported in many studies to act as a photocatalyst for the degradation of organic pollutants through radicals' reactions [39,82,83]. The existence of atmospheric oxygen and water plays a key role in the formation of hydroxyl radicals on the samples calcined at T > 200 °C [10]. It has been also previously shown that the interactions of ZnO with 2-chloroethyl ethyl sulfide result in water formation [8]. These water molecules can act as a constant source of hydroxyl anions, which can be transformed to hydroxyl radicals when reacting with the e<sup>-</sup>/h<sup>+</sup> pairs [62]. During the exposure to vapors and



Scheme 1. Proposed reactions pathways of EES and CEES adsorption and subsequent reaction process on the samples containing only the peroxide phase ( $\text{ZnO}_2$  and  $\text{Zn130}$ ).



Scheme 2. Proposed reactions scheme of EES adsorption and subsequent reaction on the samples containing the zinc oxide phase.

especially after 6 days of interactions, the powder samples gained a gel-like structure. This can be due to the condensations of the surrogates and their reaction products on the surface, as well as of the formed water molecules. All the steps of the proposed EES or CEES photo-detoxification pathways on the samples containing zinc oxide, are summarized in **Scheme 2**.

In the case of interactions of Zn300 and Zn400 with EES vapors, the first stage of the photo-degradation involves the reaction of EES with hydroxyl radicals with two possible dehydrogenation positions (Pathway B1). If  $\beta$ -carbon thioether radical were formed, its further reaction with a hydroxyl radical would lead to HEES. Since HEES was not detected in the extracts, the hydrogen is removed rather from  $\alpha$ -carbon than from  $\beta$ -carbon. Support for this are the results of Vorontsov et al. who reported that when EES interacted with TiO<sub>2</sub> at ambient conditions, the hydrogen abstraction from the  $\beta$ -carbon was the minor pathway compared to that from  $\alpha$ -carbon [84]. The second stage implicates the protonation of the above mentioned  $\alpha$ -carbon thioether radical. This formed intermediate radical cation undergoes a cleavage of the S–C bond via the reaction with a hydroxyl anion, forming ethanol and ethyl sulfide radical. The latter radical can recombine with another one resulting in DEDS or with  $\beta$ -carbon thioether radical and thus in the formation of BETE. No BETE detected either in the headspace or in the extracts further supports the hydrogen abstraction from the  $\alpha$ -carbon. Even though BETE was reported as a product of the interactions of metal (hydr)oxides with CEES, the existence of zinc oxide triggers selectively the formation of the  $\alpha$ -carbon radical. This is also supported by the results of our previously study, which showed the formation of BETE as the minor pathway when CEES vapors interacted with ferric zinc double salt [80]. Formation of DEDS was the major pathway.

On the samples consisting only of the zinc oxide phase EVS, HEES and BETE were formed as a result of interactions with CEES vapors. The formation of EVS (Pathway B2) can be attributed to the transient intermediate cyclic cation that transforms to EVS, as discussed above. It can be also formed as a result of an intermolecular electron rearrangement of  $\beta$ -carbon thioether radical with the simultaneous involvement of a hydroxyl radical. The formation of the  $\beta$ -carbon thioether radical is possible in the case of CEES, since it can be formed from the ethyl ethylsulfide cation upon its reaction with a hydroxyl radical. HEES and BETE are the result of the reaction of the  $\beta$ -carbon thioether radical with hydroxyl and ethylsulfide radicals, respectively (Pathway B3).

Zn200 has both zinc peroxide and oxide phases. The amount of EESO detected in the extracts after exposure to EES vapors was significantly smaller than those on ZnO<sub>2</sub> and Zn130, but also slightly higher than those on Zn300 and Zn400. On the contrary, the amount of DEDS was higher than those on the samples consisting of only the zinc peroxide phase, but lower than on the samples with only the zinc oxide phase. This suggests that Zn200 has the ability to catalytically degrade EES both like zinc peroxide and zinc oxide do. The same trend was found when Zn200 interacted with CEES vapors.

### 3.8. Detoxification of the CWA agent, mustard gas

The detoxification performance of the ZnO<sub>2</sub> nanoparticles was also determined against the real agent, mustard gas (HD). HD droplets were dispersed on the powdered ZnO<sub>2</sub> sample and the unreacted HD/its reactions products were extracted with acetonitrile. The conversion ratio was calculated based on the GC–MS analysis. On ZnO<sub>2</sub> it is 76.5%. This value is 26% higher than that obtained for CEES.

The analysis of the extracts by GC–MS showed only hydroxyethyl vinyl sulfide and 1,4-Dithiane as the reaction products (Fig. S4). These results suggest that hydrolysis is the predominant detoxification pathway, as was the case when the sample was exposed to CEES. The formation of the double bond implies involvement of an intermediate cyclic cation, from which 2-chloroethyl vinyl sulfide is formed. The

latter reacts further and get transformed to hydroxyethyl vinyl sulfide. It is important to mention that the detection of only two products does not exclude the possibility of the formation of other compounds. The removal of the chloride atoms from the molecule can lead to alternative products, such as thiodiglycol that might be strongly adsorbed on the surface. Another evidence that supports this possibility and the oxidative ability of ZnO<sub>2</sub> nanoparticles, is the detection of acetamide as a result of the acetonitrile oxidation.

## 4. Conclusions

Highly porous zinc peroxide nanoparticles were synthesized following a simple one-pot wet precipitation method. The results show that the ZnO<sub>2</sub> structure is stable up to 130 °C. At this temperature the sample loses micropores, and surface water, while the surface pH slightly increases. At 200 °C, zinc peroxide is partially converted to ZnO, leading to a compound where both ZnO and ZnO<sub>2</sub> phases coexist. This ZnO phase, contrarily to ZnO<sub>2</sub>, has the ability to form hydroxyl radicals at visible light irradiation. Thermal treatment above 300 °C leads to the complete transformation of the zinc peroxide nanoparticles to zinc oxide nanoparticles with the same morphology, but of a significantly lower porosity. The decomposition of the peroxide to oxide phase was monitored by XRD or Raman spectroscopy.

The capability of all samples to decompose vapors and droplets of two surrogates of mustard gas, 2-chloroethyl ethyl sulfide (CEES) and ethyl ethyl sulfide (EES) and to reactively adsorb vapors or droplets of both chemical warfare agent surrogates of mustard gas was tested. ZnO<sub>2</sub> showed the best detoxification performance for both CEES and EES compared to all other samples tested in this study, and compared to various metal oxides/hydroxides reported in the literature that have been tested at the same conditions. ZnO<sub>2</sub> also showed some level of multi-functionality, since it both adsorbed and degraded vapors and droplets of both surrogates. The surface chemistry was found to play the most crucial role, since no correlation between the weight uptake upon CEES or EES exposure and the structural parameters was found. Finally, ZnO<sub>2</sub> nanoparticles showed a high conversion ratio against the real agent mustard gas, that was 26 and 66% higher compared to the conversion ratio of the surrogates CEES and EES, respectively.

## Acknowledgements

This work was supported by ARO (Army Research Office of USA) [grant W911NF-13-1-0225] and NSF collaborative CBET [grant 1133112]. The authors would like to thank Eric Jensen for his help experimental help (ARO USAP program). Fruitful discussion with Gregory Mogilevsky is highly appreciated. D.A.G. is grateful for a partial scholarship from Onassis Foundation.

## Appendix A. Supplementary data

Supplementary data associated with this article can be found, in the online version, at <https://doi.org/10.1016/j.apcatb.2017.12.068>.

## References

- [1] T.C. Marrs, R.L. Maynard, F.R. Sidell, *Chemical Warfare Agents: Toxicology and Treatment*, 2nd ed., John Wiley & Sons, Ltd, 2007.
- [2] A. Mattsson, C. Lejon, V. Štengl, S. Bakardjieva, F. Opluštil, P.O. Andersson, L. Österlund, *Appl. Catal. B Environ.* 92 (2009) 401.
- [3] V. Štengl, V. Houšková, S. Bakardjieva, N. Murafa, M. Maříková, F. Opluštil, T. Němcová, *Mater. Charact.* 61 (2010) 1080.
- [4] A.T. Vu, S. Jiang, K. Ho, J.B. Lee, C.H. Lee, *Chem. Eng. J.* 269 (2015) 82.
- [5] M. Verma, R. Chandra, V.K. Gupta, *J. Environ. Chem. Eng.* 4 (2016) 219.
- [6] M. Verma, V.K. Gupta, V. Dave, R. Chandra, G.K. Prasad, *J. Colloid Interface Sci.* 438 (2015) 102.
- [7] A.-T. Vu, S. Jiang, K. Ho, J.B. Lee, C.-H. Lee, *Chem. Eng. J.* 269 (2015) 82.
- [8] D.A. Giannakoudakis, J.A. Arcibar-Orozco, T.J. Bandosz, *Appl. Catal. B Environ.* 174 (2015) 96.
- [9] A.-T. Vu, K. Ho, C.-H. Lee, *Chem. Eng. J.* 283 (2016) 1234.

- [10] J.A. Arcibar-Orozco, D.A. Giannakoudakis, T.J. Bandosz, *Chem. Eng. J.* 303 (2016) 123.
- [11] G.K. Prasad, B. Singh, A. Saxena, *AIChE J.* 52 (2006) 678.
- [12] Y. Luo, D.F. Ollis, *J. Catal.* 163 (1996) 1.
- [13] J.E. Mondloch, M.J. Katz, W.C. Isley III, P. Ghosh, P. Liao, W. Bury, G.W. Wagner, M.G. Hall, J.B. Decoste, G.W. Peterson, R.Q. Snurr, C.J. Cramer, J.T. Hupp, O.K. Farha, *Nat. Mater.* 14 (2015) 1.
- [14] J.B. DeCoste, G.W. Peterson, *Chem. Rev.* 114 (2014) 5695.
- [15] K. Kim, O.G. Tsay, D.a. Atwood, D.G. Churchill, *Chem. Rev.* (Washington, DC, United States) 111 (2011) 5345.
- [16] T.J. Bandosz, M. Laskoski, J. Mahle, G. Mogilevsky, G.W. Peterson, J.A. Rossin, G.W. Wagner, *J. Phys. Chem. C* 116 (2012) 11606.
- [17] J. Abelard, A.R. Wilmsmeyer, A.C. Edwards, W.O. Gordon, E.M. Durke, C.J. Karwacki, D. Troya, J.R. Morris, *J. Phys. Chem. C* 119 (2015) 365.
- [18] T.H. Mahato, B. Singh, A.K. Srivastava, G.K. Prasad, A.R. Srivastava, K. Ganesan, R. Vijayaraghavan, *J. Hazard. Mater.* 192 (2011) 1890.
- [19] G. Prasad, B. Singh, *J. Hazard. Mater.* 116 (2004) 213.
- [20] D.A. Giannakoudakis, M. Seredysh, E. Rodríguez-Castellón, T.J. Bandosz, *ChemNanoMat* 2 (2016) 268.
- [21] J.A. Arcibar-Orozco, D.A. Giannakoudakis, T.J. Bandosz, *Adv. Mater. Interfaces* 2 (16) (2015) 1500215.
- [22] C. Montoro, F. Linares, E. Quartapelle Procopio, I. Senkovska, S. Kaskel, S. Galli, N. Masciocchi, E. Barea, J.A.R. Navarro, *J. Am. Chem. Soc.* 133 (2011) 11888.
- [23] J. Zhao, D.T. Lee, R.W. Yaga, M.G. Hall, H.F. Barton, I.R. Woodward, C.J. Oldham, H.J. Walls, G.W. Peterson, G.N. Parsons, *Angew. Chem.-Int. Ed.* 55 (2016) 13224.
- [24] E. Barea, C. Montoro, J.A.R. Navarro, *Chem. Soc. Rev.* 43 (2014) 5419.
- [25] D.A. Giannakoudakis, Y. Hu, M. Florent, T.J. Bandosz, *Nanoscale Horiz.* 2 (2017) 356.
- [26] D.A. Giannakoudakis, T.J. Bandosz, *Detoxification of Chemical Warfare Agents. From WWI to Multifunctional Nanocomposite Approaches*, 1st ed., Springer International Publishing, 2018. doi:10.1007/978-3-319-70760-0.
- [27] G.W. Wagner, L.R. Procell, V.D. Henderson, D.C. Sorrick, Y.-C. Yang, *Decon Green, The Environmentally-Friendly Decontaminant*, Aberdeen Proving Ground, 2003.
- [28] G.W. Wagner, Y.-C. Yang, *Ind. Eng. Chem. Res.* 41 (2002) 1925.
- [29] Y.C. Yang, J. a Baker, J.R. Ward, *Chem. Rev.* 92 (1992) 1729.
- [30] F.M. Menger, M.J. Rourk, *Langmuir* 15 (1999) 309.
- [31] D.D. Dionysiou, M.T. Suidan, E. Bekou, I. Baudin, J.M. Laîné, *Appl. Catal. B Environ.* 26 (2000) 153.
- [32] D.D. Dionysiou, M.T. Suidan, I. Baudin, J.-M. Laîné, *Appl. Catal. B Environ.* 50 (2004) 259.
- [33] Y. Liu, C.T. Buru, A.J. Howarth, J.J. Mahle, J.H. Buchanan, J.B. DeCoste, J.T. Hupp, O.K. Farha, *J. Mater. Chem. A* 4 (2016) 13809.
- [34] X.-F. Wu, *Tetrahedron Lett.* 53 (2012) 4328.
- [35] O. Mabayoje, M. Seredysh, T.J. Bandosz, *Appl. Catal. B Environ.* 132–133 (2013) 321.
- [36] H.S. Song, M.G. Park, S.J. Kwon, K.B. Yi, E. Croiset, Z. Chen, S.C. Nam, *Appl. Surf. Sci.* 276 (2013) 646.
- [37] D.A. Giannakoudakis, T.J. Bandosz, *J. Colloid Interface Sci.* 436 (2014) 296.
- [38] S.T. Hobson, E.H. Braue, J.E.K. Lehnert, K.J. Klabunde, O.P. Koper, S. Decker, *Active Topical Skin Protectants Using Reactive Nanoparticles*, US6403653 B1, 2002.
- [39] T.H. Mahato, G.K. Prasad, B. Singh, J. Acharya, A.R. Srivastava, R. Vijayaraghavan, *J. Hazard. Mater.* 165 (2009) 928.
- [40] R. Hagel, K. Redecker, *Pat.* 2952069, 1981.
- [41] L. Ibarra, A. Marcos-Fernández, M. Alzorrriz, *Polymer (Guildf.)* 43 (2002) 1649.
- [42] L. Ibarra, M. Alzorrriz, *J. Appl. Polym. Sci.* 84 (2002) 605.
- [43] L. Ibarra, M. Alzorrriz, *Polym. Int.* 49 (2000) 115.
- [44] L. Ibarra, M. Alzorrriz, *J. Appl. Polym. Sci.* 86 (2002) 335.
- [45] F.L. Meleney, *Int. J. Orthod. Oral Surg.* 23 (1937) 932.
- [46] D.A. Sunderland, J.S. Binkley, *Radiology* 35 (1940) 606.
- [47] E.D. Volova, T. Bychatina, *Zhurnal Prikl. Khimii (Sankt-Peterburg Russ. Fed.)* 18 (1945) 172.
- [48] G. Cogne, C. R. 206 (1938) 1119.
- [49] E. Ebler, R.L. Krause, *Z. Anorg. Chem.* 71 (1911) 150.
- [50] L. Rosenthal-Toib, K. Zohar, M. Alagem, Y. Tsur, *Chem. Eng. J.* 136 (2008) 425.
- [51] M. Sun, W. Hao, C. Wang, T. Wang, *Chem. Phys. Lett.* 443 (2007) 342.
- [52] N.G. Vannerberg, *Ark. Foer Kemi* 14 (1959) 119.
- [53] V.F. Boiko, *Nauchnye Dokl. Vyss. Shkoly Khimiya I Khimicheskaya Tekhnologiya* 1 (1959) 57.
- [54] D.A. Giannakoudakis, N.A. Travlou, J. Secor, T.J. Bandosz, *Small* 13 (2017) 1601758.
- [55] A. Escobedo-Morales, R. Esparza, A. García-Ruiz, A. Aguilar, E. Rubio-Rosas, R. Pérez, *J. Cryst. Growth* 316 (2011) 37.
- [56] X. Han, R. Liu, W. Chen, Z. Xu, *Thin Solid Films* 516 (2008) 4025.
- [57] P. Ganguly, R.K. Kotnala, S. Singh, R.P. Pant, N. Singh, *Carbon* 95 (2015) 428.
- [58] Q.A. Drmosh, M.A. Gondal, Z.H. Yamani, T.A. Saleh, *Appl. Surf. Sci.* 256 (2010) 4661.
- [59] M. Thommes, K. Kaneko, A.V. Neimark, J.P. Olivier, F. Rodriguez-Reinoso, J. Rouquerol, K.S.W.W. Sing, *Pure Appl. Chem.* 87 (2015) 1051.
- [60] D.A. Giannakoudakis, J.K. Mitchell, T.J. Bandosz, *J. Mater. Chem. A* 4 (2016) 1008.
- [61] J.A. Arcibar-Orozco, T.J. Bandosz, *J. Mater. Chem. A* 3 (2015) 220.
- [62] D.A. Giannakoudakis, J.A. Arcibar-Orozco, T.J. Bandosz, *Appl. Catal. B Environ.* 183 (2016) 37.
- [63] D. Sebők, T. Szabó, I. Dékány, *Appl. Surf. Sci.* 255 (2009) 6953.
- [64] N.J. Nicholas, G.V. Franks, W.A. Ducker, *CrystEngComm* 14 (2012) 1232.
- [65] T. Andelman, Y. Gong, M. Polking, M. Yin, I. Kuskovsky, G. Neumark, S. O'Brien, *J. Phys. Chem. B* 109 (2005) 14314.
- [66] N. Uekawa, N. Mochizuki, J. Kajiwara, F. Mori, Y.J. Wu, K. Kakegawa, *Phys. Chem. Chem. Phys.* 5 (2003) 929.
- [67] H. Bai, X. Liu, *Mater. Lett.* 64 (2010) 341.
- [68] J. Wang, S. Hou, H. Chen, L. Xiang, *J. Phys. Chem. C* 118 (2014) 19469.
- [69] G. Kenanakis, D. Vernardou, N. Katsarakis, *Appl. Catal. A Gen.* 411–412 (2012) 7.
- [70] S. Mukhopadhyay, P.P. Das, S. Maity, P. Ghosh, P.S. Devi, *Appl. Catal. B Environ.* 165 (2015) 128.
- [71] P. Kubelka, F. Munk, *Z. Tech. Phys.* 12 (1931) 593.
- [72] H.G. Hecht, *J. Res. NBS A Phys. Chem.* 80 (1976) 567.
- [73] J. Tauc, *Mater. Res. Bull.* 3 (1968) 37.
- [74] W. Raza, M.M. Haque, M. Muneer, *Appl. Surf. Sci.* 322 (2014) 215.
- [75] J. Secor, V. Narinesingh, M. Seredysh, D.A. Giannakoudakis, T.J. Bandosz, R.R. Alfano, *J. Photonics Energy* 5 (2015) 53084.
- [76] C. Shifu, Z. Wei, Z. Sujuan, L. Wei, *Chem. Eng. J.* 148 (2009) 263.
- [77] V. Lakshmi Prasanna, R. Vijayaraghavan, *Langmuir* (2015) 150729122119004.
- [78] J.K. Mitchell, J.A. Arcibar-Orozco, T.J. Bandosz, *Appl. Surf. Sci.* 390 (2016) 735.
- [79] I.N. Martyanov, K.J. Klabunde, *Environ. Sci. Technol.* 37 (2003) 3448.
- [80] M. Florent, D.A. Giannakoudakis, R. Wallace, T.J. Bandosz, *J. Hazard. Mater.* 329 (2017) 141.
- [81] R. Wallace, D.A. Giannakoudakis, M. Florent, C. Karwacki, T.J. Bandosz, *J. Mater. Chem. A* 5 (2017) 4972.
- [82] E. Evgenidou, I. Konstantinou, K. Fytianos, I. Poulios, T. Albanis, *Catal. Today* 124 (2007) 156.
- [83] Y. Lai, M. Meng, Y. Yu, X. Wang, T. Ding, *Appl. Catal. B Environ.* 105 (2011) 335.
- [84] A.V. Vorontsov, E.V. Savinov, L. Davydov, P.G. Smirniotis, *Appl. Catal. B Environ.* 32 (2001) 11.